

Damage Initiation and Propagation in Composites Subjected to Low-Velocity Impact: Experimental Results, 3D Dynamic Damage Model, and FEM Simulations

JIA Wenbin, WEN Weidong*, FANG Lei

Jiangsu Province Key Laboratory of Aerospace Power System, College of Energy and Power Engineering, Nanjing University of Aeronautics and Astronautics, Nanjing 210016, P.R. China

(Received 18 September 2018; revised 26 November 2018; accepted 27 April 2019)

Abstract: A three-dimensional dynamic damage model that fits both small and large damage sizes is developed to predict impact damage initiation and propagation for each lamina of T300-carbon/epoxy laminations. First, 13 specimens of the same lamination sequence are subjected to three different impact energies (10 J, 15 J, and 20 J). After the impact, the laminates are inspected by the naked eye to observe the damage in the outer layers, and subsequently X-rayed to detect the inner damage. Next, the stress analysis of laminates subjected to impact loading is presented, based on the Hertz contact law and virtual displacement principle. Based on the analysis results, a three-dimensional dynamic damage model is proposed, including the Hou failure criteria and Camanho stiffness degradation model, to predict the impact damage shape and area. The numerical predictions of the damage shape and area show a relatively reasonable agreement with the experiments. Finally, the impact damage initiation and propagation for each lamina are investigated using this damage model, and the results improve the understanding of the impact process.

Key words: composites; impact; three-dimensional dynamic damage model; impact damage initiation and propagation

CLC number: V258; TB332

Document code: A

Article ID: 1005-1120(2019)03-0488-12

0 Introduction

Composites are being used increasingly in the aerospace and automotive fields, owing to their specific mechanical properties and lightweightness. However, the susceptibility to low-velocity impact damage, which often occurs in routine maintenance, is regarded as the major factor that can reduce the strength of composites significantly^[1]. Moreover, the impact damage in forms of matrix cracking, matrix crushing, and delamination is difficult to detect by visual inspection because the damage is often embedded in the laminate. This barely visible impact damage accounts for the material stiffness degradation of the laminate. Therefore, it is essential to develop a reliable model to predict damage initiation and propagation for each lamina accurately.

A large number of low-velocity impact experiments for composites have been performed to study impact damage forms, shapes, and evolution. Sayer et al.^[2] examined the impact damage forms of glass-carbon/epoxy hybrid composites with different impact faces, i.e. glass-carbon (GC) and carbon-glass (CG). By visual inspection, the study showed that matrix cracking and delamination were the primary damage forms in the glass layers while matrix cracking and fiber breaking dominated the carbon layers. However, the inner damage cannot be detected by visual inspection. Xu^[3] X-rayed the impacted composites to detect the damage shapes under different impact energies for T300-carbon/polyimide. The results indicated that the damage shape was approximately a circle under small impact energy while an elliptical damage shape occurred under larger impact

*Corresponding author, E-mail address: gswwd@nuaa.edu.cn.

How to cite this article: JIA Wenbin, WEN Weidong, FANG Lei. Damage Initiation and Propagation in Composites Subjected to Low-Velocity Impact: Experimental Results, 3D Dynamic Damage Model, and FEM Simulations[J]. Transactions of Nanjing University of Aeronautics and Astronautics, 2019, 36(3):488-499.

<http://dx.doi.org/10.16356/j.1005-1120.2019.03.013>

energy. Minak et al.^[4] used acoustic emission (AE) to investigate the damage propagation of T300-carbon/epoxy composites, and evaluated the impact damage evolution by combining a sentry function and AE.

However, it is time consuming and costly to detect the inner damage experimentally. Therefore, several researchers have proposed several analytical models to predict impact damage initiation and propagation. Ashish et al.^[5] presented an analytical model for the response of rectangular, symmetric, laminated composite plates subjected to low-velocity impact and damage initiation in the form of yarn/fiber and breakage was predicted. Feng et al.^[6] used progressive damage models in combination with cohesive interface elements to predict the structural response and failure mechanisms of composite laminates subjected to low-velocity impact. The potential of this simulation approach for correctly predicting the through-thickness distribution of internal damage was examined in the study. Lopes et al.^[7] considered the physical progressive failure behavior of fibers, matrix, and interfaces between plies, and used the finite element method to predict low-velocity impact events on composite laminates. The computational effort resulted in the reliable predictions of the impact dynamics, impact footprint, locus and size of delamination, matrix cracks, and fiber damage. Periyasamy et al.^[8] used the commercially available software ABAQUS to study the response of individual layers, with an elastic-plastic model for the metal layer and a user-defined constitutive model via a VUMAT subroutine for the composite layer. Menna et al.^[9] performed a numerical simulation of low-velocity impact tests on glass fabric/epoxy laminates through the LS-DYNA finite element (FE) code. Two laminates of different thicknesses were subjected to a transverse impact at different energy levels and modeled by FE. Caputo et al.^[10] proposed a numerical technique to describe the damage initiation and propagation of impact damages in composite structures based on advanced material models and selected failure criteria. Naik et al.^[11] used a modified Hertz law and quadratic failure criteria to predict the in-plane and interlaminar failure initiation

of different polymer-matrix composites subjected to low-velocity impacts. Aymerich et al.^[12] used an FE model based on cohesive interface elements to simulate complex three-dimensional damage patterns in composite laminates subjected to low-velocity impact. Esrail et al.^[13] presented an efficient method to predict the type, size, and location of damage in impacted quasi-isotropic composite laminates. The method used the peak force during impact obtained from energy balance, a Hertzian contact formulation, and energy minimization to determine the complete state of stress in the laminate. Zheng et al.^[14] used an elasto-plastic contact law that considers permanent indentation and damage effects, to study small-mass impact on laminated composite plates. Maio et al.^[15] used a progressive damage model to predict the delamination damage induced by low-velocity impacts in a laminated composite. Shi et al.^[16] employed the FE method to simulate the behavior of the composite subjected to low-velocity impacts. Interface cohesive elements were inserted between plies with appropriate mixed-mode damage laws to model delamination. Sun et al.^[17] employed the cohesive zone model to simulate delamination, matrix cracks, and their interactions, and presented the predictive damage with different levels in detail. Roger et al.^[18] used both layer and interface damage initiation and propagation models based on the Hashin and Benzeggagh-Kenane criteria for the numerical simulations. Zangani et al.^[19] used a numerical model based on explicit FE analysis to simulate the behavior of the sandwich panels subjected to low-velocity impact. The numerical model has been validated in terms of the failure behavior of the panel and the variation in the contact force after the initial peak load corresponding to flexural failure. Abir et al.^[20] developed a damage model that distinguished the different damage forms of fiber breaking, matrix cracking, and delamination. A continuum damage mechanics (CDM) approach was proposed to model fiber breaking and matrix cracking, and cohesive interface elements were used to simulate delamination. Donadon et al.^[21] and Falzon et al.^[22-24] proposed a three-dimensional (3D) CDM-based model, including nonlinear shear behavior, ply friction,

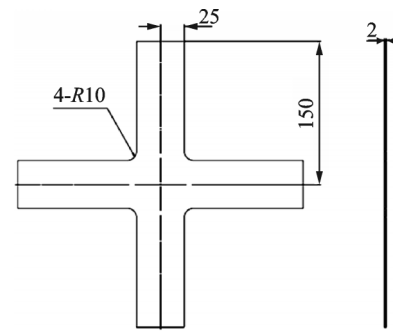
and damage irreversibility, to investigate the damage propagation in the inner layers. Similarly, Bouvet et al.^[25] and Hongkarnjanakul et al.^[26] developed a damage model that focused on damage propagation in the inner layers by combined CMD with the image capture method. More recently, Tan et al.^[27] presented a 3D damage model that included an updated damage initiation criterion and a unified matrix-dominated damage law. These damage models can predict impact damage initiation and propagation accurately. However, the predicted results become inaccurate when the damage size is large^[28].

Therefore, the aim of this paper is to develop a 3D dynamic damage model that fits both small and large damage sizes to predict impact damage initiation and propagation for each lamina. First, laminates with the same stacking sequence were subjected to three different vertical impact energies (10 J, 15 J, and 20 J). After the impact, the laminates were inspected by the naked eye to observe the damage in the outer layers, followed by X-ray to detect the inner damage. Next, a three-dimensional dynamic damage model is proposed, including the Hou^[29] failure criteria and Camanho^[30] stiffness degradation model, to predict the impact damage shape and area. The numerical predictions of the damage shape and area show a relatively reasonable agreement with the experimental data. Finally, the impact damage initiation and propagation for each lamina were investigated using the damage model, and the results improved the understanding of the impact process.

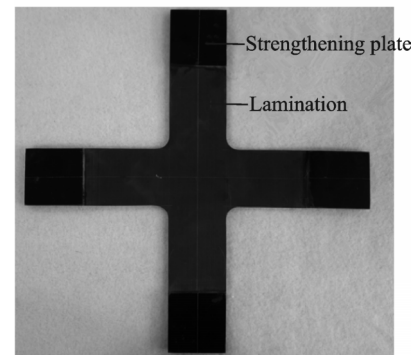
1 Materials and Methods

1.1 Materials

This section describes the specimen properties and experimental setup. Thirteen cruciform specimens were tested. The aim of the cruciform design is to investigate the biaxial residual strength after impact in a further study that will not be discussed herein. The geometrical schematic diagram and actual structure of the specimen are shown in Fig.1. The specimens were produced in an autoclave by overlapping 17 unidirectional plies of T300 carbon fiber-



(a) Geometrical schematic diagram



(b) Actual structure

Fig.1 Specimen

epoxy prepreg and the lamination sequence is $[(0/90)_4/\bar{0}]_s$. Each lamina is 0.118 mm thick and its mechanical properties are shown in Table 1.

Table 1 T300 carbon-epoxy material properties

Material property	Value
Young's modulus in the fiber direction E_1 / GPa	132
Young's modulus in the transverse direction E_2 / GPa	8.8
Young's modulus in the normal direction E_3 / GPa	8.8
Poisson's ratio ν_{12}	0.021
Poisson's ratio ν_{13}	0.021
Poisson's ratio ν_{23}	0.315
Shear modulus G_{12} / GPa	5.3
Shear modulus G_{13} / GPa	5.3
Shear modulus G_{23} / GPa	5.3
Tensile strength in the fiber direction X_T / MPa	1 593
Compressive strength in the fiber direction X_C / MPa	1 238
Tensile strength in the transverse direction Y_T / MPa	58
Compressive strength in the transverse direction Y_C / MPa	242
Tensile strength in the through-thickness direction Z_T / MPa	58
Shear strength for matrix cracking S_{12} / MPa	99.7
Shear strength for matrix cracking S_{m23} / MPa	99.7
Shear strength for delamination S_{13} / MPa	99.7
Shear strength concerning fiber failure S_l / MPa	189

1.2 Test procedure

The specimen was clamped in the test bed of the impact testing machine KS-150LC (Fig.2), and subjected to a low-velocity impact produced by a cylindrical impactor with a hemispherical head striking the center along the vertical direction. Fig.3 shows the clamping system and shape of the impactor.



Fig.2 Impact testing machine

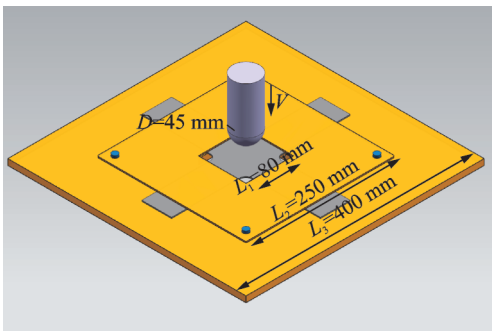


Fig.3 Illustration of the impact testing setup

Accidental handling damages such as “tool drop” often occurs during maintenance and the impact energy ranges from 10 J to 20 J. Therefore, three impact energies (10 J, 15 J, and 20 J) were chosen for the impact tests. The value of impact energy was set by the console (Fig.2) in the testing machine and controlled by the guide rail (Fig.2). The initial velocity under different impact energies can be calculated by

$$v_i = \sqrt{\frac{2E_i}{m_1}} \quad i = 1, 2, 3 \quad (1)$$

where m_1 (1.5 kg) and E_i (10 J, 15 J, and 20 J) rep-

resent the impactor mass and impact energy, respectively.

The specimens’ numbering uses the E - Z form. E represents the impact energy and Z represents the sequence number of the specimen under the same impact energy. For example, 10 J-2 presents the second specimen under 10 J impact energy.

The experimental plan consisted of two stages:

(1) Thirteen specimens were tested under three different vertical impact energies. The arrangement is shown in Table 2.

Table 2 Arrangement of specimens

Specimen	Initial velocity/ ($m \cdot s^{-1}$)	Number of specimens
10 J-Z(1-4)	3.7	4
15 J-Z(1-4)	4.5	4
20 J-Z(1-5)	5.2	5

(2) After the impact, the specimens were first inspected by the naked eye to observe the damage in the outer layers, and subsequently X-rayed to detect the inner damage.

2 Experimental Results

Impact damage was examined by both visual inspection and X-ray. Only the visual inspection results are shown in this section, and the X-ray results will be presented in Section 4.2.

Fig.4 shows the visual inspection of the damage for different impact energies and Table 3 presents the data for the damage size.

Fig.4 shows that (1) indentation is barely visible on the top surface for all the specimens despite different impact energies; (2) for the back surface of the specimens, fiber breaking and delamination are the primary damage forms for the 20 J impact energy while only fiber breaking is dominant for the 10 J and 15 J impact energies. Table 3 indicates that (1) the indentation depth for the three impact energies (10 J, 15 J, and 20 J) ranges from 0.1 mm to 0.3 mm, suggesting no distinct difference in indentation depth among the three impact energies; (2) for the back surface of the specimens, the height of swelling (ranging from 0.1 mm

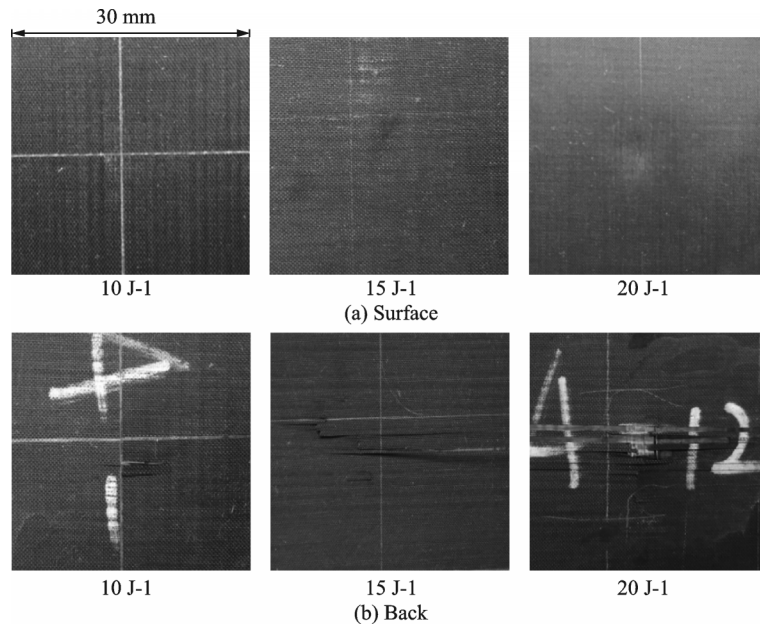


Fig.4 Visual inspection of impact damage

Table 3 Damage size of visual inspection

Specimen	Indentation depth /mm	Swelling height /mm	Length of fiber breaking / mm
10 J-Z(1-4)	0.1—0.15	0.1—0.15	5—7
15 J-Z(1-4)	0.1—0.2	0.3—0.5	15—24
20 J-Z(1-4)	0.2—0.3	0.7—1.0	20—29

to 1 mm) and the length of fiber breaking (ranging from 5 mm to 29 mm) increase with impact energy.

3 Damage Model

Based on the Hertz contact law and virtual displacement principle, the stress analysis process of laminates subjected to impact loading is derived. Further, based on the derivation results, a three-dimensional dynamic damage model, including the Hou failure criteria and Camanho stiffness degradation model, is proposed to predict the impact damage shape and area.

3.1 Analytical model

To obtain the stress distribution at every moment during the impact process, a 3D dynamic model was developed to investigate the impact dynamics.

A system consisting of a laminate and impactor is shown in Fig.5, and the origin of the coordinates is located in the middle of the short side. We assume the element displacement and stress of the laminate

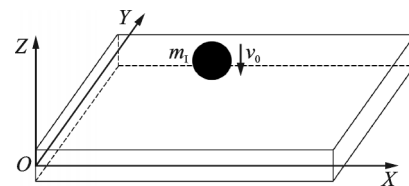


Fig.5 Coordinates of laminate and impactor

as ${}^t u_i$ and ${}^t \sigma_{ij}$ at moment t , respectively. The equilibrium equation is given by

$${}^t \sigma_{ij,j} - \rho {}^t \ddot{u}_i - \mu {}^t \dot{u}_i = 0 \quad (2)$$

where ρ , μ , ${}^t \dot{u}_i$, and ${}^t \ddot{u}_i$ represent the density, damping coefficient, and the first and second derivatives with respect to time, respectively.

We assume that the force per unit area at the force boundary (S_σ) is ${}^t \bar{T}_i$ at moment t , thus the force boundary condition is given by

$${}^t \sigma_{ij} n_j - {}^t \bar{T}_i = 0 \quad (3)$$

According to the Galerkin method, the equivalent integration form combining Eqs.(2), (3) can be written as

$$\int_V \delta u_i ({}^t \sigma_{ij,j} - \rho {}^t \ddot{u}_i - \mu {}^t \dot{u}_i) dV - \int_{S_\sigma} \delta u_i ({}^t \sigma_{ij} n_j - {}^t \bar{T}_i) dS = 0 \quad (4)$$

The nonlinear geometric equation in the form of the Green strain tensor is given by

$${}^t\epsilon_{ij} = B_{ij} {}^tU_{ij} = \frac{1}{2} ({}^t u_{i,j} + {}^t u_{j,i} + {}^t u_{k,i} {}^t u_{k,j}) \quad (5)$$

The physical equation is given by

$${}^t\sigma_{ij} = {}^{t-\Delta t}\bar{Q}_{ijkl} {}^t\epsilon_{kl} \quad (6)$$

where ${}^{t-\Delta t}\bar{Q}_{ijkl}$ represents the lamina's elastic matrix in the Cartesian coordinate at moment $t - \Delta t$.

When the angle between the fiber direction and Cartesian coordinate equals θ (shown in Fig.6), ${}^{t-\Delta t}\bar{Q}_{ijkl}$ can be defined as

$${}^{t-\Delta t}\bar{Q}_{ijkl} = T {}^{t-\Delta t}Q T^T \quad (7)$$

where T and ${}^{t-\Delta t}Q$ represent the coordinate-transfor-

$$T = \begin{bmatrix} \cos^2\theta & \sin^2\theta & 0 & 0 & 0 & -2\sin\theta\cos\theta \\ \sin^2\theta & \cos^2\theta & 0 & 0 & 0 & 2\sin\theta\cos\theta \\ 0 & 0 & 1 & 0 & 0 & 0 \\ 0 & 0 & 0 & \cos\theta & \sin\theta & 0 \\ 0 & 0 & 0 & -\sin\theta & \cos\theta & 0 \\ \sin\theta\cos\theta & -\sin\theta\cos\theta & 0 & 0 & 0 & \cos^2\theta - \sin^2\theta \end{bmatrix} \quad (8)$$

$${}^{t-\Delta t}Q = \begin{bmatrix} {}^{t-\Delta t}Q_{11} & {}^{t-\Delta t}Q_{12} & {}^{t-\Delta t}Q_{13} & 0 & 0 & 0 \\ {}^{t-\Delta t}Q_{12} & {}^{t-\Delta t}Q_{22} & {}^{t-\Delta t}Q_{23} & 0 & 0 & 0 \\ {}^{t-\Delta t}Q_{13} & {}^{t-\Delta t}Q_{23} & {}^{t-\Delta t}Q_{33} & 0 & 0 & 0 \\ 0 & 0 & 0 & {}^{t-\Delta t}Q_{44} & 0 & 0 \\ 0 & 0 & 0 & 0 & {}^{t-\Delta t}Q_{55} & 0 \\ 0 & 0 & 0 & 0 & 0 & {}^{t-\Delta t}Q_{66} \end{bmatrix} \quad (9)$$

where ${}^{t-\Delta t}Q_{ij}$ is the elastic constant function that degrades at moment $t - \Delta t$.

Substituting Eq.(6) into Eq.(4) yields

$$\int_V (\delta\epsilon_{ij} {}^{t-\Delta t}\bar{Q}_{ij} {}^t\epsilon_{ij} + \delta u_i \rho {}^t\ddot{u}_i + \delta u_i \mu {}^t\dot{u}_i) dV = \int_{S_s} \delta u_i {}^t\bar{T}_i dS \quad (10)$$

The element displacement is given by

$$u^e = N a^e \quad (11)$$

where u^e , a^e , and N represent the element displacement, nodal displacement, and displacement shape function, respectively.

Substituting Eqs.(5), (11) into Eq.(4), we obtain the element's equation of motion

$$M^e \ddot{a}^e(t) + C^e \dot{a}^e(t) + K^e a^e(t) = F^e(t) \quad (12)$$

where

$$M^e = \int_{V^e} \rho N^T N dV, C^e = \int_{V^e} \mu N^T N dV$$

$$K^e = \int_{V^e} B^T \bar{Q} B dV, F^e = \int_{S_s^e} N^T N dS$$

Further, the laminate's equation of motion is given by

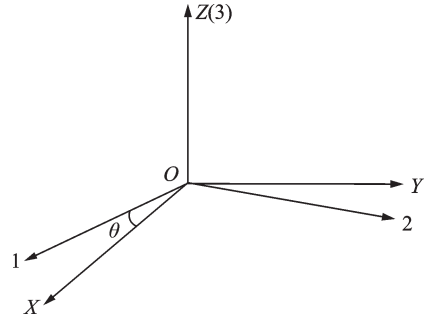


Fig.6 Angle between fiber direction and Cartesian coordinate

mation matrix and elastic matrix in the principal coordinate, and are given as follows

$$M\ddot{a}(t) + C\dot{a}(t) + Ka(t) = F(t) \quad (13)$$

where $M, C, K, a(t)$, and $F(t)$ represent the laminate's mass matrix, damping matrix, stiffness matrix, node displacement vector, and node internal force, respectively.

The laminate's equation of motion is obtained, and the impactor's equation of motion can be deduced.

For the impactor, we assume the initial displacement and velocity as $w_1 = 0$ and $\dot{w}_1 = v_0$, respectively. The equation of motion is given by

$$m_1 \ddot{w}_1^2 + F = 0 \quad (14)$$

where F represents the reactive force of $F(t)$.

According to the Hertzian contact law, F can be calculated by

$$\alpha F = \begin{cases} k\alpha^{1.5} & \text{Loading} \\ F_m \left(\frac{\alpha - \alpha_0}{\alpha_m - \alpha_0} \right)^q & \text{Unloading} \end{cases} \quad (15)$$

where k and q are constant; F_m and α_m represent the maximum force and indentation depth during load process, respectively; α_0 represents the unrecover-

able indentation depth; and α is a variable of the indentation depth. k and α_0 are expressed as follows

$$k = \frac{4}{3} \sqrt{R} \left(\frac{1 - \nu^2}{E} + \frac{1}{E_3} \right)^{-1} \quad (16)$$

$$\alpha_0 = \begin{cases} \alpha_m \left[1 - \left(\frac{\alpha_{cr}}{\alpha_m} \right)^{\frac{2}{5}} \right] & \alpha_m > \alpha_{cr} \\ F_m \left(\frac{\alpha - \alpha_0}{\alpha_m - \alpha_0} \right)^q & \alpha_m \leq \alpha_{cr} \end{cases} \quad (17)$$

where α_{cr} is constant, R , ν , and E represent the radius, Poisson ration, and elastic modulus of the impactor, respectively, and E_3 represents the lamina's elastic modulus in the thickness direction. α can be given by

$$\alpha(t) = w_1(t) - u_s(x_s, y_s, t) \quad (18)$$

where (x_s, y_s) is the coordinate of the contact element.

Substituting F into the laminate's equation of motion (Eq. (13)), the nodal displacement at moment t ($a^e(t)$) can be calculated. Subsequently, substituting $a^e(t)$ into Eq. (11), the element displacement at moment t ($u^e(t)$) can be calculated. Finally, the laminate's element strain (ϵ^t) and stress (σ^t) can be obtained by substituting $u^e(t)$ into the geometric and physical equations (Eqs. (5), (6), respectively).

When the calculation is completed, the damage will be detected by the Hou^[29] failure criteria. Once the damage is found, the lamina's elastic matrix updates by the Camanho^[30] stiffness degradation model, where ${}^{t-\Delta t} \bar{Q}_{ijkl}$ turns into ${}^t \bar{Q}_{ijkl}$. The laminate's stress-strain relationship subsequently becomes

$${}^t \sigma_{ij} = {}^{t-\Delta t} \bar{Q}_{ijkl} {}^t \epsilon_{kl} \quad (19)$$

It is obvious that the laminate's stress will change once damage occurs. Therefore, ${}^t \sigma_{ij}$ will be iterated using Eqs. (12), (5) and (19) until no damages are detected by the Hou^[29] failure criteria.

3.2 Failure criteria

The Hou^[29] failure criteria was employed, in which five damage modes were considered: fiber tensile breaking, fiber compressive breaking, matrix cracking, matrix crushing, and delamination.

(1) Fiber tensile failure ($\sigma_{11} \geq 0$)

$$\left(\frac{\sigma_{11}}{X_T} \right)^2 + \left(\frac{\sigma_{12}}{S_f} \right)^2 + \left(\frac{\sigma_{13}}{S_f} \right)^2 = 1 \quad (20)$$

(2) Fiber compressive failure ($\sigma_{11} < 0$)

$$\left(\frac{\sigma_{11}}{X_C} \right)^2 + \left(\frac{\sigma_{12}}{S_f} \right)^2 + \left(\frac{\sigma_{13}}{S_f} \right)^2 = 1 \quad (21)$$

(3) Matrix cracking ($\sigma_{22} \geq 0$)

$$\left(\frac{\sigma_{22}}{Y_T} \right)^2 + \left(\frac{\sigma_{12}}{S_{12}} \right)^2 + \left(\frac{\sigma_{23}}{S_{m23}} \right)^2 = 1 \quad (22)$$

(4) Matrix crushing ($\sigma_{22} < 0$)

$$\frac{1}{4} \left(\frac{-\sigma_{22}}{S_{12}} \right)^2 + \left(\frac{\sigma_{12}}{S_{12}} \right)^2 + \frac{Y_C^2 \sigma_{22}}{4 S_{12}^2 Y_C} - \frac{\sigma_{22}}{Y_C} = 1 \quad (23)$$

(5) Delamination

$$\left(\frac{\sigma_{33}}{Z_T} \right)^2 + \left(\frac{\sigma_{13}}{S_{13}} \right)^2 + \left(\frac{\sigma_{23}}{S_{123}} \right)^2 = 1 \quad (24)$$

where σ_{11} is the stress in the fiber direction, σ_{22} the stress in the transverse direction, σ_{33} the stress in the through-thickness direction, σ_{12} the shear stress in the plane of fiber and transverse directions, σ_{13} the shear stress in the plane of through-thickness and fiber directions, σ_{23} the shear stress in the plane transverse and through-thickness plane, X_T the tensile strength in the fiber direction, X_C the compressive strength in the fiber direction, Y_T the tensile strength in the transverse direction, Y_C the compressive strength in the transverse direction, Z_T the tensile strength in the through-thickness direction, S_{12} the shear strength in the fiber and transverse plane, S_{13} the shear strength in the through-thickness and fiber plane, S_f the shear strength involving fiber failure, S_{m23} the shear strength for matrix cracking in the transverse and through-thickness plane, and S_{123} the shear strength for delamination in the transverse and through-thickness plane.

3.3 Stiffness degradation model

To consider the stiffness degradation induced by the impact damage, the Camanho^[30] stiffness degradation model was employed, as shown in Table 4.

Table 4 Stiffness degradation model

Damage mode	Parameter	Degradation factor
Fiber tensile failure	$E_1, E_2, G_{12}, G_{13}, G_{23}, \nu_{12}, \nu_{13}, \nu_{23}$	0.07
Fiber compressive failure	$E_1, E_2, G_{12}, G_{13}, G_{23}, \nu_{12}, \nu_{13}, \nu_{23}$	0.14
Matrix cracking	E_2, G_{12}, G_{23}	0.2
Matrix crushing	E_2, G_{12}, G_{23}	0.4
Delamination	$E_3, G_{13}, G_{23}, \nu_{13}, \nu_{23}$	0

4 FEM and Results

An FE was developed in ANSYS LS-DYNA based on the damage model described above, with ANSYS parametric design language (APDL). Moreover, the damage shape and area were evaluated by comparing the FEM results with X-ray results.

4.1 FE model

Solid 164 was used for the 3D modeling and this element was defined by eight nodes of the following degrees of freedom at each node: Translations, velocities, and accelerations in the nodal x , y , and z directions. To assign orthotropic material properties (listed in Table 1), the element coordinate was changed from Cartesian to principal coordinate. The impactor was modeled as a rigid body and its acceleration was assigned as $g(9.8\text{ m/s}^2)$. The impactor was placed at a small distance (h_0) above the surface of the specimen and the velocity at this displacement can be calculated by

$$v_0 = \sqrt{\frac{2(E_i - m_1gh_0)}{m_1}} \tag{25}$$

Furthermore, the analyses were performed in the nonlinear geometric behavior. Fig.7 shows the

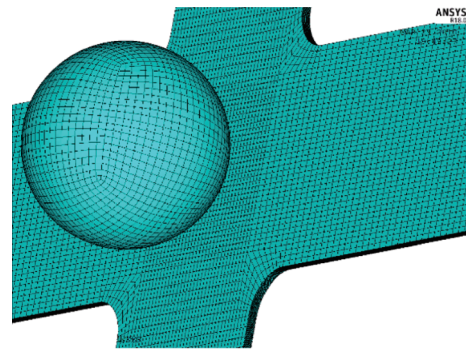


Fig.7 Meshed modeling of the lamination and impactor

meshed modeling of the lamination and impactor. The impactor was modeled as a sphere.

First, for each element, five damage forms (including fiber tensile breaking, fiber compressive breaking, matrix cracking, matrix crushing and delamination) were detected by the Hou failure criteria (Section 3.2). Subsequently, once one of the damage forms was detected, the element was printed with the corresponding color (shown in last row of Fig.8) and its material properties were modified by the stiffness degradation model (Section 3.3).

4.2 FEM results (compared with X-ray)

Fiber breaking was evaluated by the comparison between the FEM and X-ray results, as it was

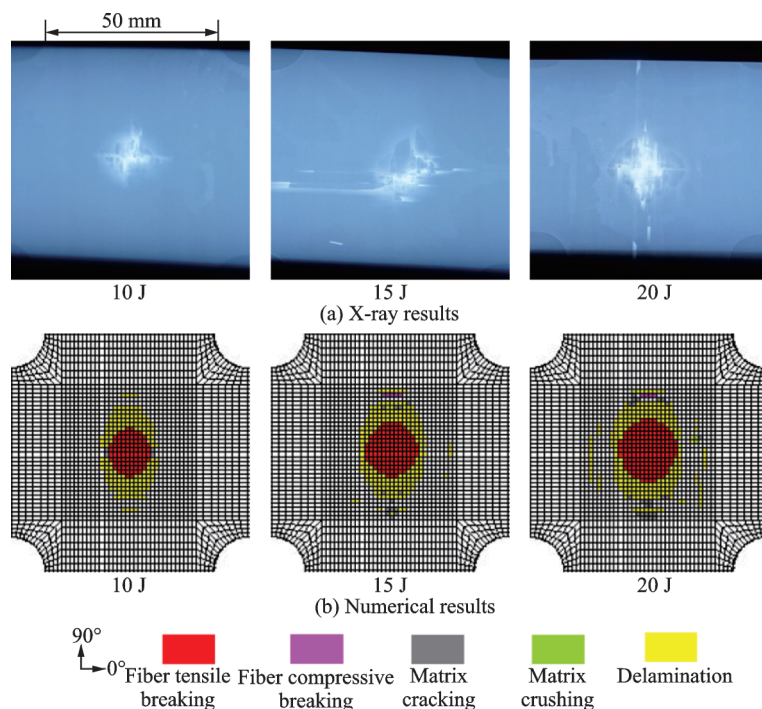


Fig.8 Damage shape under three impact energies

the major cause of strength reduction.

Fig.8 shows the comparison of damage shape between X-ray results and FEM results. The X-ray result shows that despite the three different impact energies, the damage yields a shape that is similar to an ellipse. To investigate the inner damage, the total damage elements were projected on the surface lamina and the total damage is shown in second row of Fig.8. The FEM results suggest that the damage shape of fiber breaking (red and purple elements) is predicted satisfactorily.

Table 5 shows the comparison results of the damage area from the X-ray and FEM results, and Fig.9 shows the relationship between the damage area and impact energy.

Table 5 Damage areas for X-ray and predicted results

Impact energy / J	X-ray area / mm ²	Predicted area / mm ²	Error / %
10	196.98	181.25	-7.99
15	267.88	243.75	-9.01
20	346.36	329.69	-4.81

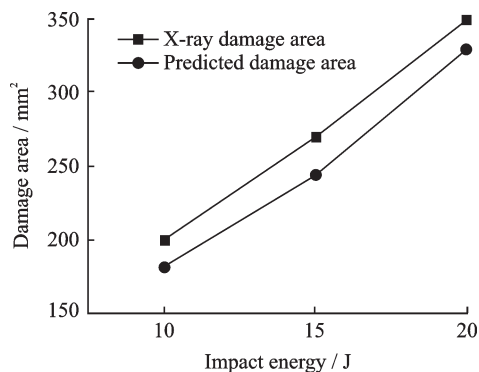


Fig.9 Relationship between damage area and impact energy

5 Damage Initiation and Propagation

Because the inner damage is difficult to detect, it is important to be able to predict the initiation and propagation for each lamina. The aim of the following sections is to investigate the damage propagation including the five damage forms using the damage model proposed above.

The initiation and propagation of the five dam-

age forms were investigated by the FEM. For each lamina, the damage was detected with increasing contact time and the FEM results are shown in Fig.10. Because no obvious difference was found between the damage propagation under the three impact energies, the damage under 15 J was chosen as a representative. Layers 1 and 17 represent the surface and bottom laminas, respectively.

Fig.10 (a) shows that when the contact time reaches 0.628 ms, damage initiation occurs, where only layers 1 and 2 exhibit fiber compressive breaking and delamination, respectively. Fig.10 (b) indicates that delamination and matrix cracking occur from layers 13 to 17 at the moment $t = 1.252$ ms while only delamination appears in layer 12. The damage reaches the maximum at the moment $t = 1.876$ ms, as shown in Fig.10 (c). Fig.10 (c) suggests that damage has propagated in all layers, where the primary damage forms are fiber compressive breaking, matrix cracking, and delamination from layers 1 to 3, while fiber tensile breaking and delamination dominate layers 10 to 17 and only delamination in the middle layers.

Moreover, Fig.10 also indicates the following:

(1) Damage initiation occurs in the top layers and subsequently in the bottom layers. Finally, damage appears in the middle layers with damage propagation along the thickness direction.

(2) For the top layers, fiber compressive breaking is always the primary damage form during the impact process, and the damage shape is elliptical.

(3) For the middle layers, delamination and matrix cracking occur first, and fiber tensile breaking appears in the lower layers with time. Moreover, all the three damage forms are dumbbell shaped.

(4) For the bottom layers, dumbbell-shaped delamination occurs first; subsequently, elliptical fiber tensile breaking appears with time.

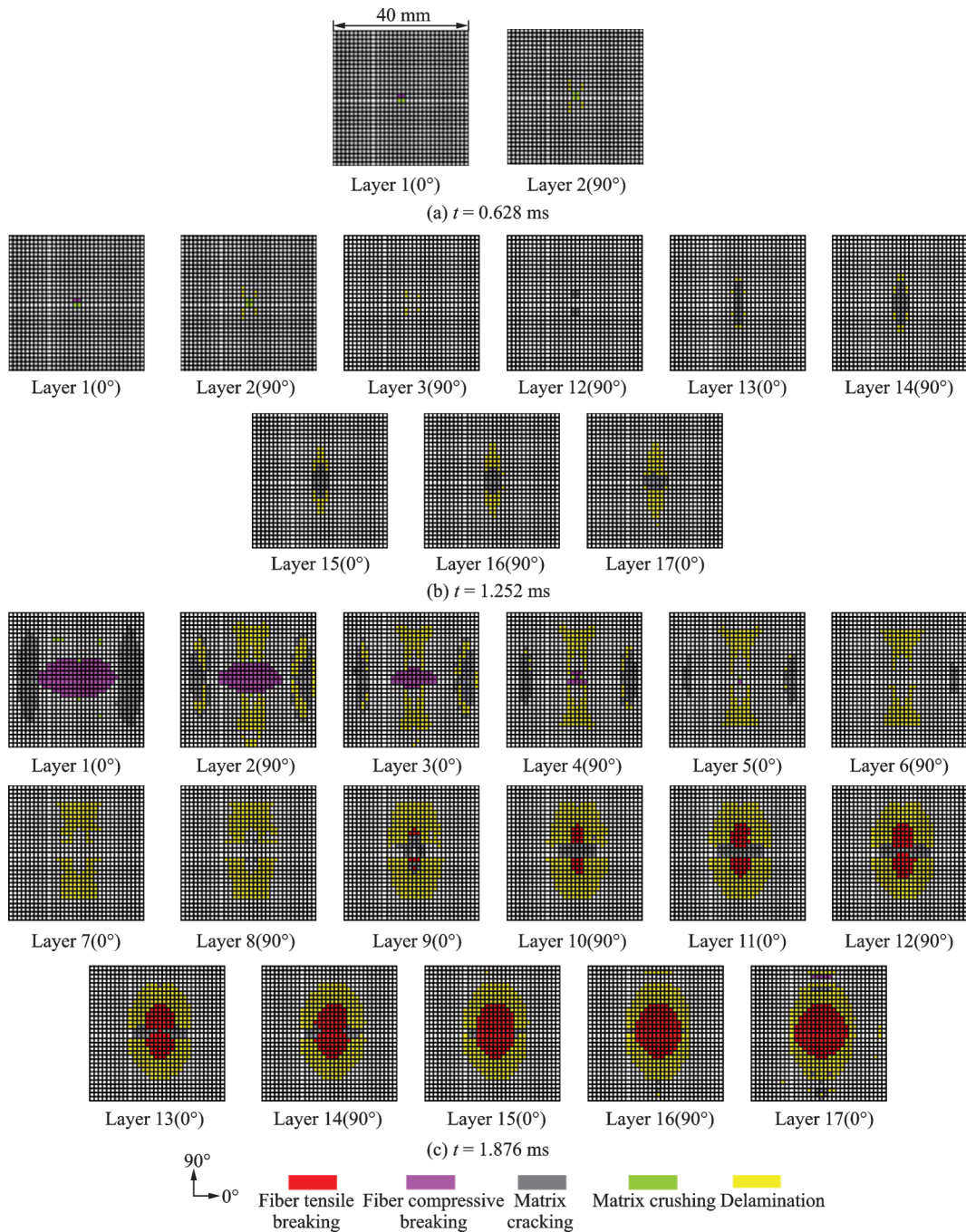


Fig.10 Initiation and propagation of five damage forms

6 Conclusions

A 3D dynamic damage model that fitted both small and large damage sizes was developed in this study to predict the impact damage initiation and propagation for each lamina of T300-carbon/epoxy laminations.

Based on the Hertz contact law and virtual displacement principle, a 3D dynamic damage model, including the Hou failure criteria and Camanho stiff-

ness degradation model, was used to predict the impact damage shape and area. The numerical predictions of the damage shape and area indicated a relatively reasonable agreement with the experiments.

The impact damage initiation and propagation for each lamina were investigated using this damage model and the results are as follows:

- (1) Damage initiation occurred in surface layers and subsequently in the bottom layers; subsequently, damage propagated in the middle layers

along the thickness direction.

(2) The primary damage form was elliptical fiber breaking in the surface and bottom layers while dumbbell-shaped fiber tensile breaking and delamination dominated the middle layers.

However, some differences still existed between the numerical predictions and X-ray results, implying that it is worth refining the model further using the X-ray results for improved accuracy and increased applicability. Nevertheless, the effect of these differences on impact damage initiation and propagation must be investigated in future studies.

References

- [1] ABRATE S. Impact on composite structures [M]. UK: Cambridge University Press, 2005: 1-24.
- [2] SAYER M, BEKTAŞ N, SAYMAN O. An experimental investigation on the impact behavior of hybrid composite plates[J]. *Compos Struct*, 2010, 92(5): 1256-1262.
- [3] XU Ying. Research on impact damage of laminates and fatigue life of impacted laminates [D]. Nanjing: Nanjing University of Aeronautics and Astronautics, 2007. (in Chinese)
- [4] MINAK G, ABRATE S, GHELLI D. Residual torsional strength after impact of CFRP tubes[J]. *Composites Part B Engineering*, 2010, 41(8): 637-645.
- [5] ASHISH M, NAIK N K. Failure initiation in composite structures under low velocity impact: Analytical studies[J]. *Compos Struct*, 2010, 92(2): 436-444.
- [6] FENG D, AYMERICH F. Finite element modelling of damage induced by low velocity impact on composite laminates [J]. *Compos Struct*, 2014, 108: 161-171.
- [7] LOPES C S, CAMANHO P P, GÜRDAL Z, et al. Low-velocity impact damage on dispersed stacking sequence laminates. Part ii: Numerical simulations [J]. *Compos Sci Technol*, 2009, 69(7): 937-947.
- [8] PERIYASAMY M, CHAI G B. A layer-wise behavioral study of metal based interplay hybrid composites under low velocity impact load [J]. *Compos Struct*, 2014, 117: 17-31.
- [9] MENNA C, ASPRONE D, CAPRINO G, et al. Numerical simulation of impact tests on GFRP composite laminates [J]. *Int J Impact Eng*, 2011, 38(8): 677-685.
- [10] CAPUTO F, De LUCA A, LAMANNA G, et al. Numerical study for the structural analysis of composite laminates subjected to low velocity impact [J]. *Compos Part B: Eng*, 2014, 67: 296-302.
- [11] NAIK N K, MEDURI S. Polymer-matrix composites subjected to low-velocity impact: Effect of laminate configuration [J]. *Compos Sci Technol*, 2001, 61(10): 1429-1436.
- [12] AYMERICH F, DORE F, PRIOLO P. Simulation of multiple delaminations in impacted cross-ply laminates using a finite element model based on cohesive interface elements [J]. *Compos Sci Technol*, 2009, 69(11): 1699-1709.
- [13] ESRAIL F, KASSAPOGLOU C. An efficient approach for damage quantification in quasi-isotropic composite laminates under low speed impact [J]. *Compos Part B: Eng*, 2014, 61: 116-126.
- [14] ZHENG D, BINIENDA W K. Effect of permanent indentation on the delamination threshold for small mass impact on plates [J]. *Int J Solids Struct*, 2007, 44(25): 8143-8158.
- [15] MAIO L, MONACO E, RICCI F, et al. Simulation of low velocity impact on composite laminates with progressive failure analysis [J]. *Compos Struct*, 2013, 103: 75-85.
- [16] SHI Y, SWAIT T, SOUTIS C. Modelling damage evolution in composite laminates subjected to low velocity impact [J]. *Compos Struct*, 2012, 94(9): 2902-2913.
- [17] SUN X C, WISNOM M R, HALLETT S R. Interaction of inter- and intralaminar damage in scaled quasi-static indentation tests: Part 2—Numerical simulation [J]. *Compos Struct*, 2016, 136: 727-742.
- [18] LEMANLE S, ROGER P, GARNIER C, et al. Finite element simulation of low velocity impact damage on an aeronautical carbon composite structure [J]. *Applied Composite Materials*, 2017, 23(6): 1-14.
- [19] ZANGANI D, ROBINSON M, GIBSON A G. Energy absorption characteristics of web-core sandwich composite panels subjected to drop-weight impact [J]. *Applied Composite Materials*, 2008, 15(3): 139-156.
- [20] ABIR M R, TAY T E, RIDHA M. Modelling damage growth in composites subjected to impact and compression after impact [J]. *Composite Struct*, 2017, 168: 13-25.
- [21] DONADON M V, IANNUCCI L, FALZON B G, et al. A progressive failure model for composite laminates subjected to low velocity impact damage [J]. *Computers & Structures*, 2008, 86(11/12): 1232-1252.
- [22] FAGGIANI A, FALZON B G. Predicting low-velocity impact damage on a stiffened composite panel [J].

- Composites Part A: Applied Science and Manufacturing, 2010, 41(6): 737-749.
- [23] FALZON B G, APRUZZESE P. Numerical analysis of intralaminar failure mechanisms in composite structures. Part I: FE implementation[J]. Compos Struct, 2011, 93(2): 1039-1046.
- [24] FALZON B G, APRUZZESE P. Numerical analysis of intralaminar failure mechanisms in composite structures. Part II: Applications [J]. Compos Struct, 2011, 93(2): 1047-1053.
- [25] BOUVET C, RIVALLANT S, BARRAU J J. Low velocity impact modeling in composite laminates capturing permanent indentation [J]. Composites Science and Technology, 2012, 72(16): 1977-1988.
- [26] HONGKARNJANAKUL N, BOUVET C, RIVALLANT S. Validation of low velocity impact modelling on different stacking sequences of CFRP laminates and influence of fiber failure [J]. Composite Structures, 2013, 106: 549-559.
- [27] TAN W, FALZON B G, CHIU L N S, et al. Predicting low velocity impact damage and Compression-after-impact (CAI) behavior of composite laminates [J]. Composites Part A, 2015, 71: 212-226.
- [28] ABRATE S. Dynamic deformation, damage and fracture in composite materials and structures[M]. [S.l.]: Woodhead Pub Ltd, 2016: 1-22.
- [29] HOU J P, PETRINIC N, RUIZ C. Prediction of impact damage in composite plates [J]. Composites Science & Technology, 2000, 60(2): 273-281.
- [30] CAMANHO P P, MATTHEWS F L. A progressive damage model for mechanically fastened joints in composite laminates[J]. J Compos Mater, 1999, 33: 2248-2280.

Authors Mr. JIA Wenbin received the B. S. degree in flight vehicle propulsion engineering and M.S. degree in avia-

tion engineering from Nanjing University of Aeronautics and Astronautics in 2012 and 2016, respectively. And now he is a doctoral student from College of Energy and Power Engineering, Nanjing University of Aeronautics and Astronautics. His research is focused on structure of advanced composite materials.

Prof. WEN Weidong has been engaged in teaching and scientific research on structure, strength and vibration in College of Energy and Power Engineering, Nanjing University of Aeronautics and Astronautics since 1985. His research has focused on structural strength and design of advanced composite materials, structural strength and fatigue of advanced high temperature materials, structural reliability and optimal design, structural vibration, structural fretting fatigue.

Prof. FANG Lei received the M. S. degree in mechanics from Johns Hopkins University and the Ph.D. degree in applied science and mechanics from Pennsylvania State University in 1988 and 1992, respectively. He is leading professor of 1000 Talents Plan and currently a professor of College of Energy and Power Engineering, Nanjing University of Aeronautics and Astronautics. His research has focused on structural strength and integrity, mechanical behavior analysis of advanced structural materials, fatigue damage and life assessment of power machinery, structural dynamics and damage detection of power machinery, vibration and vibration control of power machinery structure and reliability analysis and optimization of power machinery structure.

Author contributions Mr. JIA Wenbin designed the study, compiled the models, conducted the experiment, interpreted the results, and wrote the manuscript. Prof. WEN Weidong contributed to the analysis and background of the study. Prof. FANG Lei contributed to the background of the study.

Conflicts interests The authors declare no competing interests.

(Production Editor: Zhang Huangqun)